APPLIED OPTICS

Single-pixel computational ghost imaging with helicity-dependent metasurface hologram

Hong-Chao Liu,[1]* Biao Yang,[1] Qinghua Guo,[1,2] Jinhui Shi,[1,2,3] Chunying Guan,[1,3] Guoxing Zheng,[1,4] Holger Mühlenbernd,[5] Guixin Li,[1,6] Thomas Zentgraf,[5] Shuang Zhang[1]*

Different optical imaging techniques are based on different characteristics of light. By controlling the abrupt phase discontinuities with different polarized incident light, a metasurface can host a phase-only and helicity-dependent hologram. In contrast, ghost imaging (GI) is an indirect imaging modality to retrieve the object information from the correlation of the light intensity fluctuations. We report single-pixel computational GI with a high-efficiency reflective metasurface in both simulations and experiments. Playing a fascinating role in switching the GI target with different polarized light, the metasurface hologram generates helicity-dependent reconstructed ghost images and successfully introduces an additional security lock in a proposed optical encryption scheme based on the GI. The robustness of our encryption scheme is further verified with the vulnerability test. Building the first bridge between the metasurface hologram and the GI, our work paves the way to integrate their applications in the fields of optical communications, imaging technology, and security.

INTRODUCTION

Metasurfaces are composed of arrays of anisotropic light scatterers (for example, optical antennas) with subwavelength size and spacing on a flat and ultrathin surface (*1*–*6*). By locally engineering the phase and polarization of the incident light with the antennas' structure, metasurfaces can imitate many functionalities of common optical elements but with subwavelength resolution (*1*–*15*). In recent work, reflective metasurfaces fabricated with metallic nanorods (*16*–*18*), as well as the transmissive metasurfaces composed of metallic/dielectric antennas (*19*–*23*), successfully achieved metasurface holograms and metalens devices with a high efficiency and broadband nature, which marked a great step toward real-world applications. In reflective metasurface holograms (*17*, *18*), each nanorod represents an image pixel and gives a locally abrupt phase change ±2φ to the incident light, where φ is the orientation of the nanorod. This ±2φ phase change takes different signs when the incident beam varies from left circularly polarized (LCP) to right circularly polarized (RCP) light, which leads to helicity-dependent images of the metasurface hologram (*18*).

Independent of the phase and polarization state of light waves, ghost imaging (GI) is an indirect imaging approach to acquire the object information through the correlation calculations of light intensity fluctuations of two beams: one (object beam) passes through the object and is detected by a single-pixel detector, and the other (reference beam) does not interact with the object and is recorded by a multipixel detector with spatial resolution (*24*–*26*). GI was first observed with entangled photon pairs and viewed as a unique quantum phenomenon (*27*). Later, it was experimentally demonstrated that GI could also be achieved with a classical light source (*28*), which thus sparked considerable studies of its physical nature and relevant applications (*29*–*53*). In particular, a scheme based on the classical nature of GI, called computational GI (*50*), was proposed to apply computational intensity fluctuation patterns to replace the reference beam measurements, which therefore only required a single-pixel detector and largely simplified the experimental setup in comparison to the traditional two-detector GI (*50*, *51*). In computational GI, the object image is recovered by the correlation between the single-pixel detected intensity and the computational patterns, instead of the correlation between the object beam and reference beam. In principle, computational GI is in common with the so-called single-pixel camera technique not only in their experimental system (that is, a single-pixel detector with projected light patterns or random arrays) but also in the image reconstruction processes and algorithms (*39*, *50*).

By integrating two different imaging techniques, here, we report single-pixel computational GI with reflective metasurface holography. On the basis of the helicity-dependent property of the metasurface and computational GI technique, an optical encryption scheme is further proposed. With different image reconstruction algorithms, the quality of helicity-dependent ghost images and the vulnerability of the optical encryption are carefully investigated in both numerical simulation and experiment. Our work introduces the fascinating role of the submillimeter and high-efficiency metasurface into the GI technique, which broadens and deepens the applications of both metasurfaces and GI in the fields of optical communications, imaging technology, and security.

RESULTS

For the experimental study of the single-pixel computational GI with reflective metasurfaces, we use a setup as shown in Fig. 1A. After passing through a polarizer and a quarter-wave plate, the circularly polarized He-Ne laser beam of wavelength $\lambda = 632.8$ nm and diameter $D = 0.4$ mm is incident onto the metasurface with a 10° incident angle. The reflective metasurface with high efficiency is fabricated in a three-layer structure with a size of 333.3 μm × 333.3 μm and nanorod pixel dimensions of 300 nm × 300 nm, as shown in Fig. 1 (B and C) [see also Materials and Methods and the study of Zheng *et al.* (*17*)]. Reflected by the metasurface, the holographic image is then projected onto a

[1]School of Physics and Astronomy, University of Birmingham, Birmingham B15 2TT, UK. [2]SZU-NUS Collaborative Innovation Center for Optoelectronic Science and Technology, Key Laboratory of Optoelectronic Devices and Systems of Ministry of Education and Guangdong Province, College of Optoelectronic Engineering, Shenzhen University, Shenzhen 518060, China. [3]Key Laboratory of In-Fiber Integrated Optics of Ministry of Education, College of Science, Harbin Engineering University, Harbin 150001, China. [4]School of Electronic Information, Wuhan University, Wuhan 430072, China. [5]Department of Physics, University of Paderborn, Warburger Straße 100, Paderborn D-33098, Germany. [6]Department of Materials Science and Engineering, Southern University of Science and Technology, Shenzhen 518055, China. *Corresponding author. Email: h.liu@bham.ac.uk (H.-C.L.); s.zhang@bham.ac.uk (S.Z.)

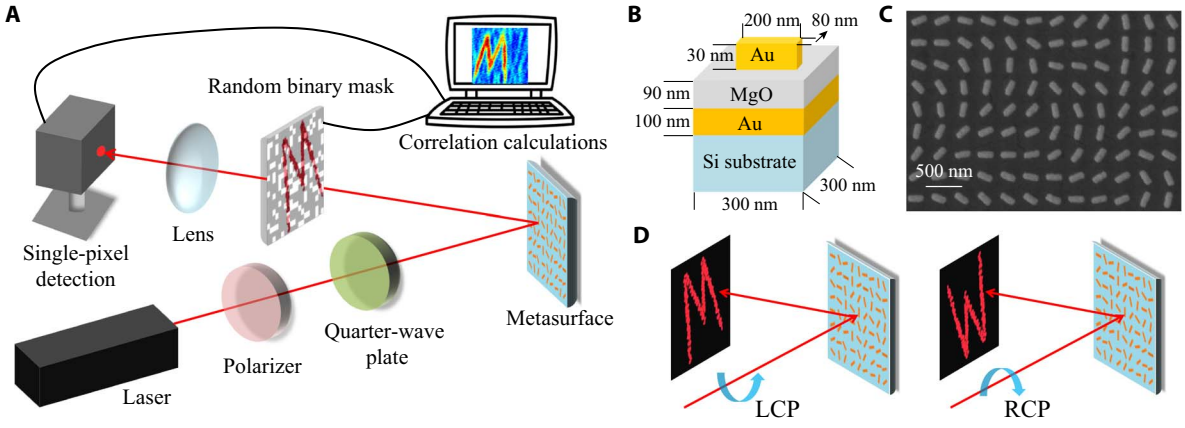

Fig. 1. Experimental setup and metasurface structure. (**A**) Schematic experimental setup of computational GI with reflective metasurface. (**B**) One-pixel cell structure of the metasurface. (**C**) Scanning electron microscopy image of the metasurface nanorod structure. (**D**) Schematic diagram of reflective metasurface hologram with LCP and RCP light.

51 pixel × 51 pixel random binary mask ($X^{m\times m}$) with a size of 145.35 mm × 145.35 mm. Next, the beam intensity passing through the random binary mask is detected by a camera, which plays the role of a bucket detector (or a single-pixel detector), meaning that only the total intensity Y arriving at the camera plane is recorded in each measurement. On the basis of the correlation theory, the holographic image can be recovered by correlation calculations between $\{X_N^{m\times m}\}$ and $\{Y_N\}$ after N times sampling measurements. Usually, a larger N leads to a better imaging quality. As shown in Fig. 1D, it is important to note that the metasurface exhibits an interesting behavior that its holographic images are spatially inverted for different helical polarization states, that is, $I(x, y)$ for LCP and $I(-x, -y)$ for RCP incident light in the holographic imaging plane. This is due to the helicity-dependent property of the metasurface (*18*). In Fig. 2A, the original image is a character "*M*." Therefore, one will observe a holographic image *M* for LCP and a "*W*" for RCP incident light, as shown in Fig. 1D.

In GI technique, the correlation algorithm mainly determines the efficiency of the image reconstruction process. Here, using the metasurface holographic image as the GI target, three different correlation algorithms [that is, standard GI, differential GI (DGI), and compressive GI (CGI) algorithm] are compared with each other. According to the standard GI, the object information can be retrieved with the second-order intensity correlation function defined as (*37*, *50*)

$$G^{(2)}(x,y) = \frac{1}{N}\sum_{i=1}^{N}\left[Y_i - \langle Y\rangle\right]X_i(x,y) \quad (1)$$

where Y_i is the bucket signal of the beam interacting with the object in the *i*th measurement. $\langle \dots \rangle$ represents the average value of N measurements. $X_i(x, y)$ is the intensity distribution of the reference beam in the xy plane, which develops into a random binary array $X_i^{m\times m}$ in the computational GI case. Developing from the definition in Eq. 1, the new differential bucket signal in the DGI algorithm is defined as (*52*)

$$Y_i^{\mathrm{DGI}} = Y_i - \frac{\langle Y\rangle}{\langle X\rangle}X_i \quad (2)$$

where $X_i = \int X_i(x, y)dxdy$ is the total intensity of the reference beam or the sum of the random binary array $X_i^{m\times m}$.

On the basis of the sparsity of the signal, a signal processing technique called compressive sensing was introduced (*54*, *55*). Recently, different improved compressive sensing algorithms, such as match pursuit, greedy basis pursuit, and iterative reweighted least squares, were developed (*56*). Because of its high efficiency in signal and image processing, compressive sensing has been widely applied to different fields, including transform imager, radio astronomy, and inversed synthetic aperture radar (*56*–*58*). As an important application of compressive sensing, the computational CGI has a quite different algorithm from the standard GI and DGI algorithms above. In computational CGI, the random binary array $X_i^{m\times m}$ is reshaped into a row vector ($1 \times K$, $K = m \times m$), and the set $\{X_N^{m\times m}\}$ of N measurements is rewritten as a two-dimensional matrix A ($N \times K$). Meanwhile, the set of bucket signals $\{Y_N\}$ is expressed as a column vector Y^{CGI} ($N \times 1$). Assuming that the image is sparse in matrix A, it can be reconstructed by solving the convex optimization program as (*38*, *51*)

$$T^{\mathrm{CGI}} = |T|,\ \min\|T\|_1 \text{ subject to } Y^{\mathrm{CGI}} = AT \quad (3)$$

where T^{CGI} is the recovered image information, T is the GI target information, and $\|T\|_1$ is the L_1 norm of T.

Assuming that the incident beam is LCP and sampling measurements $N = 2601$, Fig. 2 (D to F) shows the simulation results with standard GI, DGI, and CGI algorithms. Here, Fig. 2C with 51 × 51 pixels acts as the GI target, which is the intensity representation of the holographic image in Fig. 2B. As can be seen from Fig. 2D, it is difficult to recognize the character *M* recovered from standard GI algorithm, indicating that it cannot overcome the measurement's Nyquist limit ($N = 51 \times 51 = 2601$), and more measurements ($N \gg 2601$) are required to obtain a clear image (*51*). As shown in Fig. 2 (E and F), although DGI presents a great improvement compared with the standard GI, its background noise is still much larger than the CGI case. To quantitatively estimate the recovered image quality, we introduce the peak signal-to-noise ratio (PSNR) as

$$\mathrm{PSNR} = 10\log_{10}\left(\frac{\mathrm{MAX}^2}{\mathrm{MSE}}\right) \quad (4)$$

where MAX is the maximum possible pixel value of the image; in our case, this value is MAX = 255. MSE is the mean square error given by

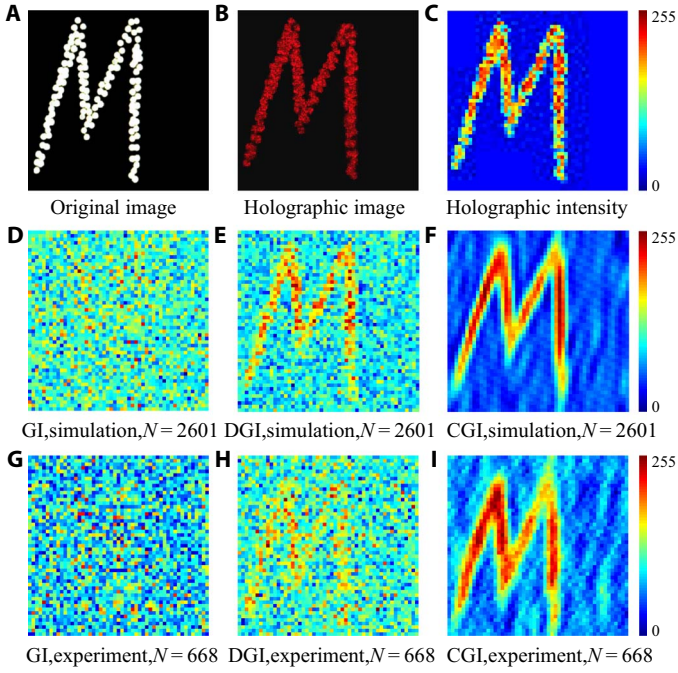

Fig. 2. Simulated and experimental results with different GI algorithms. (**A**) Original image. (**B**) Experimental metasurface holographic image. (**C**) The intensity distribution of metasurface holographic image in 51 × 51 pixels. Simulated reconstructed image (51 × 51 pixels) from holographic image with different algorithms: (**D**) standard GI, (**E**) DGI, and (**F**) CGI. The sampling measurement is set to N = 51 × 51 = 2601 in the simulation. Experimentally reconstructed image with different algorithms: (**G**) GI, (**H**) DGI, and (**I**) CGI. The incident light is LCP, and the sampling measurement N is 668 in the experiment.

$\frac{1}{m\times m}\sum_{i,j}\left[T_{\mathrm{re}}(x_i,y_j)-T(x_i,y_j)\right]^2$, where $T_{\mathrm{re}}(x_i,y_j)$ and $T(x_i,y_j)$ are the pixel values of the recovered image (for example, Fig. 2, D to F) and the GI target (for example, Fig. 2C), respectively (*38*, *51*). The PSNR values of simulated GI, DGI, and CGI are calculated as 7.83, 9.88, and 11.78 dB, respectively. Furthermore, with an LCP incident light and measurement number N = 668, experimentally recovered images in Fig. 2 (G to I) are consistent with the simulations, which confirms the great advantage of CGI in the imaging reconstruction. On the basis of the above results, we therefore use the CGI as the reconstruction algorithm in the helicity-dependent GI experiment below.

Figure 3 (A to H) shows the experimentally reconstructed holographic images for different polarized beams and different sampling measurements. For both LCP and RCP cases, the outlines of the recovered image are roughly recognized when N > 200. As the measurement number N increases, the recovered images become clearer, as shown in Fig. 3 (A to H). Their corresponding PSNR values in Fig. 3I also exhibit a marked enhancement when N > 200. Much less than the Nyquist limit (N = 2601), a few measurements (N = 650) successfully result in an identifiable experimental image. Because of the helicity-dependent functionality of the metasurface, the holographic images show a spatially inverted intensity distribution for LCP and RCP light, leading to the helicity-dependent recovered ghost images, as shown in Fig. 3 (D and H). Taking advantage of this helicity-dependent property, metasurface holography therefore hosts unique merits as a GI target in applications. As an example, below, we provide a design of an optical encryption scheme based on the CGI in combination with a helicity-dependent metasurface hologram.

Privately, Alice intends to send Bob an image, for simplicity, only consisting of the number sequence "1608" as shown in Fig. 4A. We assume that they have a shared dictionary $\{X_N^{m\times m}\}$ (that is, the set of random binary matrix). Alice first encodes the image into a submillimeter metasurface. After she reaches a safe place together with the tiny metasurface, Alice uses an LCP or RCP light to decrypt it into a holographic image, then re-encrypt this holographic image into a series of bucket detected intensity values $\{Y_N\}$ by using the dictionary $\{X_N^{m\times m}\}$. After receiving the $\{Y_N\}$ information from Alice, Bob can successfully rebuild the image with $\{X_N^{m\times m}\}$ by using the CGI algorithm. If LCP light is used in the whole encryption process, Bob will obtain the number 1608, whereas the sequence "8091" is decrypted by Bob when the encrypted light is RCP. Supposing an extreme case that both the dictionary $\{X_N^{m\times m}\}$ and the whole $\{Y_N\}$ message are stolen, the eavesdropper can thus completely reconstruct the encoded image if the GI target is a conventional transmissive or reflective object (*37*). However, adopting a helicity-dependent metasurface holographic image as the GI target, the polarization state of incident light will provide another security lock to the image information. During the encryption process, Alice can arbitrarily change the polarization states of incident light on the Nth bucket detection (for example, LCP for $\{Y_{N'}\}$ and RCP for $\{Y_{N''}\}$), as shown in Fig. 4A. Therefore, without knowing the relationship between the polarization state and the Nth bucket detection (that is, the key as indicated by the yellow arrow in Fig. 4A), the image reconstruction process will fail even if the dictionary $\{X_N^{m\times m}\}$ and message $\{Y_N\}$ have been 100% stolen. Figure 4A shows the simulation result that the eavesdropper will obtain a blurry and overlapped recovered image after he steals 100% dictionary $\{X_N^{m\times m}\}$ and message $\{Y_N\}$ but without knowing the key of light polarization information. In addition, Alice can also apply different incident light intensity for LCP and RCP cases, which will enhance the complexity of the decryption from the eavesdropper.

Experimentally, the vulnerability of the optical encryption scheme is tested with a different key mismatch ratio when the incident beam is LCP, as shown in Fig. 4 (B to D). As can be seen, the eavesdropper has to steal at least 60% of the keys to recover a recognizable image. This ratio is much higher than the one (10%) with the standard GI algorithm in the study of Clemente *et al.* (*37*), indicating a great advantage of CGI in optical encryption. Figure 4 (E to G) shows the recovered image with different key ratios of LCP and RCP light. The image becomes blurry when the LCP component exceeds 30% of the total key number. When the key ratio of the LCP and RCP light takes 1:1, a blurry and overlapped recovered image is obtained, which is consistent with the simulation result in Fig. 4A and indicates the important role of the helicity-dependent metasurface hologram in upgrading the computational GI encryption scheme.

DISCUSSION

Apart from the helicity-dependent property, the metasurface can also host a nonlinearly dependent holography (*59*), where the LCP and RCP incident light with the wavelength of the second or third harmonic will create different holographic images. As a GI target, this nonlinear holography of the metasurface is thereby expected to enhance the security of optical encryption based on the computational GI scheme, similar to the case as illustrated in Fig. 4. Moreover, with its very compact physical size, the metasurface is easy to hide and transport; therefore, it has another advantage in security transportation compared with other normal objects or conventional optical devices, such as liquid-crystal spatial light modulators (SLM) and digital micromirror devices, which

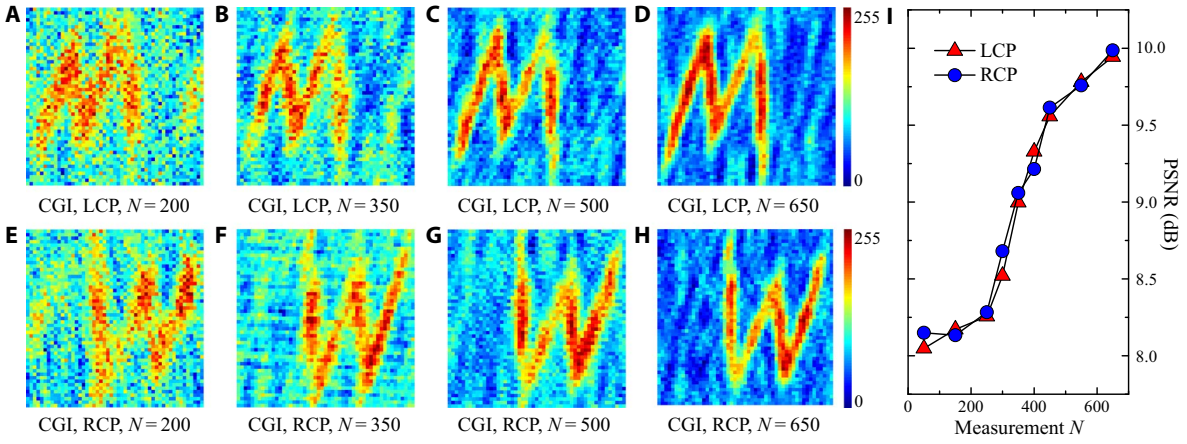

Fig. 3. Experimentally recovered images (51 × 51 pixels) and their PSNR with CGI algorithm. The polarization state of incident light is LCP in the first row and RCP in the second row. The sampling measurements were as follows: N = 200 in (**A**) and (**E**), N = 350 in (**B**) and (**F**), N = 500 in (**C**) and (**G**), and N = 650 in (**D**) and (**H**). (**I**) Experimental PSNR at different measurement N for both LCP and RCP cases.

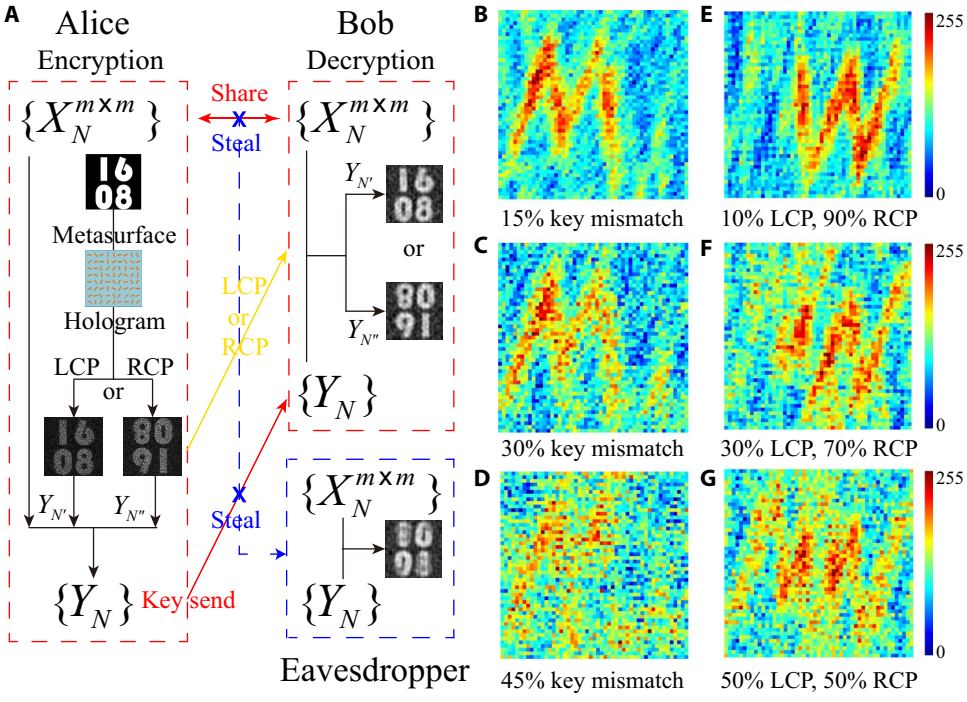

Fig. 4. Optical encryption proposal and its vulnerability test. (**A**) Scheme of the optical encryption based on CGI with helicity-dependent metasurface hologram. All holographic and CGI recovered images come from the simulation with a 101 pixel × 101 pixel 1608 original image and measurement N = 8000. Experimentally reconstructed image with LCP light: (**B**) 15% key mismatch, (**C**) 30% key mismatch, and (**D**) 45% key mismatch. Their corresponding recovered hologram image with 0% key mismatch is Fig. 3C. Experimentally reconstructed image with different key ratios of LCP and RCP light: (**E**) 10% LCP versus 90% RCP, (**F**) 30% LCP versus 70% RCP, and (**G**) 50% LCP versus 50% RCP. The key numbers of RCP light in (E) to (G) are fixed at 500.

nevertheless have merits in being electrically tunable and ready to use. Compared with the pixel size (3.8 to 36 μm) of a standard SLM, the small pixel size (~300 nm) of the metasurface leads to the generation of a holographic image with a much higher resolution than an SLM (usually 1024 × 768 pixels). Because of its small pixel size, the metasurface can generate the holographic image with a much wider projected angle, which enables the image to directly project onto the random mask in a short distance without a lens. This direct and close projection simplifies the setup of the single-pixel imaging system and effectively avoids the possible imaging distortion generated by the focus lens, in comparison to the computational GI setup for a normal object.

In addition, it is worth mentioning that the encryption process in Fig. 4 can also be achieved by a normal multipixel camera. By using the computer-generated random masks, one can mimic the single-pixel imaging process as we exactly did in the simulation shown in Fig. 2. The single-pixel intensity detection in the experiment would be replaced by a simulation process with additional calculations (that is, projecting multipixel image detected by the normal camera to the different

computer-generating random masks and then summing up the intensity of each pixel to obtain the total intensity).

Our work observes the helicity-dependent ghost images by taking the reflective and high-efficiency metasurface holographic image as a GI target, which develops into an upgraded optical encryption scheme with stronger robustness than the standard GI. Beyond the imaging target, metasurface holographic images also have the potential to serve as a component of the single-pixel imaging system, that is, the projected light patterns or the role of random masks in the future when the rotation of each nanorod on the metasurface can be controlled dynamically. For this purpose, a transmissive high-efficiency (~100%) metasurface with dielectrics (*22*, *23*, *60*, *61*) will be a better choice to integrate a compact and powerful single-pixel camera system.

MATERIALS AND METHODS

The reflective metasurface with high efficiency and broadband nature was designed according to the classical Gerchberg-Saxton algorithm (*62*) and fabricated in a three-layer structure. The bottom layer was a 130-nm-thick gold film on the silicon substrate. The middle layer was a 90-nm-thick MgF_2 film acting as a Fabry-Pérot cavity. The top layer was a gold nanorod (length × width × thickness = 200 nm × 80 nm × 30 nm) array with 1111 × 1111 pixels (or nanorods) and with pixel dimensions of 300 nm × 300 nm. Detailed simulations and experiments on the high efficiency and broadband responses of the metasurface were found in the study of Zheng *et al.* (*17*). The 51 pixel × 51 pixel random binary masks were printed on the regular paper sheets with a size of 145.35 mm × 145.35 mm. To enhance the mask sparsity, the transmissive pixel–to–untransmissive pixel ratio of the random binary masks was set to 1:99. The distance between the metasurface and random binary mask was fixed at 600 mm to project the largest holographic image M onto the random binary mask. The detector (Huawei Honor 5X) was 150 mm away from the random binary mask, and the focal length of its internal lens was set to 3 mm. In the CGI reconstruction, the orthogonal matching pursuit method was applied in the program (*56*, *63*).

REFERENCES AND NOTES

1. N. I. Zheludev, Y. S. Kivshar, From metamaterials to metadevices. *Nat. Mater.* **11**, 917–924 (2012).
2. A. V. Kildishev, A. Boltasseva, V. M. Shalaev, Planar photonics with metasurfaces. *Science* **339**, 1232009 (2013).
3. N. Yu, F. Capasso, Flat optics with designer metasurfaces. *Nat. Mater.* **13**, 139–150 (2014).
4. N. Meinzer, W. L. Barnes, I. R. Hooper, Plasmonic meta-atoms and metasurfaces. *Nat. Photonics* **8**, 889–898 (2014).
5. A. E. Minovich, A. E. Miroshnichenko, A. Y. Bykov, T. V. Murzina, D. N. Neshev, Y. S. Kivshar, Functional and nonlinear optical metasurfaces. *Laser Photonics Rev.* **9**, 195–213 (2015).
6. L. Zhang, S. Mei, K. Huang, C.-W. Qiu, Advances in full control of electromagnetic waves with metasurfaces. *Adv. Opt. Mater.* **4**, 818–833 (2016).
7. A. Shaltout, J. Liu, V. M. Shalaev, A. V. Kildishev, Optically active metasurface with non-chiral plasmonic nanoantennas. *Nano Lett.* **14**, 4426–4431 (2014).
8. Q. Wang, E. T. F. Rogers, B. Gholipour, C.-M. Wang, G. Yuan, J. Teng, N. I. Zheludev, Optically reconfigurable metasurfaces and photonic devices based on phase change materials. *Nat. Photonics* **10**, 60–65 (2016).
9. N. Yu, P. Genevet, M. A. Kats, F. Aieta, J.-P. Tetienne, F. Capasso, Z. Gaburro, Light propagation with phase discontinuities: Generalized laws of reflection and refraction. *Science* **334**, 333–337 (2011).
10. X. Ni, N. K. Emani, A. V. Kildishev, A. Boltasseva, V. M. Shalaev, Broadband light bending with plasmonic nanoantennas. *Science* **335**, 427 (2012).
11. S. Sun, Q. He, S. Xiao, Q. Xu, X. Li, L. Zhou, Gradient-index meta-surfaces as a bridge linking propagating waves and surface waves. *Nat. Mater.* **11**, 426–431 (2012).
12. X. Yin, Z. Ye, J. Rho, Y. Wang, X. Zhang, Photonic spin Hall effect at metasurfaces. *Science* **339**, 1405–1407 (2013).
13. N. Shitrit, I. Yulevich, E. Maguid, D. Ozeri, D. Veksler, V. Kleiner, E. Hasman, Spin-optical metamaterial route to spin-controlled photonics. *Science* **340**, 724–726 (2013).
14. E. Hasman, N. Davidson, A. A. Friesem, Efficient multilevel phase holograms for CO_2 lasers. *Opt. Lett.* **16**, 423–425 (1991).
15. D. Lin, P. Fan, E. Hasman, M. L. Brongersma, Dielectric gradient metasurface optical elements. *Science* **345**, 298–302 (2014).
16. W. T. Chen, K.-Y. Yang, C.-M. Wang, Y.-W. Huang, G. Sun, I.-D. Chiang, C. Y. Liao, W.-L. Hsu, H. T. Lin, S. Sun, L. Zhou, A. Q. Liu, D. P. Tsai, High-efficiency broadband meta-hologram with polarization-controlled dual images. *Nano Lett.* **14**, 225–230 (2013).
17. G. Zheng, H. Mühlenbernd, M. Kenney, G. Li, T. Zentgraf, S. Zhang, Metasurface holograms reaching 80% efficiency. *Nat. Nanotechnol.* **10**, 308–312 (2015).
18. D. Wen, F. Yue, G. Li, G. Zheng, K. Chan, S. Chen, M. Chen, K. F. Li, P. W. H. Wong, K. W. Cheah, E. Y. B. Pun, S. Zhang, X. Chen, Helicity multiplexed broadband metasurface holograms. *Nat. Commun.* **6**, 8241 (2015).
19. L. Huang, X. Chen, H. Mühlenbernd, H. Zhang, S. Chen, B. Bai, Q. Tan, G. Jin, K.-W. Cheah, C.-W. Qiu, J. Li, T. Zentgraf, S. Zhang, Three-dimensional optical holography using a plasmonic metasurface. *Nat. Commun.* **4**, 2808 (2013).
20. X. Ni, A. V. Kildishev, V. M. Shalaev, Metasurface holograms for visible light. *Nat. Commun.* **4**, 2807 (2013).
21. P. Genevet, F. Capasso, Holographic optical metasurfaces: A review of current progress. *Rep. Prog. Phys.* **78**, 024401 (2015).
22. A. Arbabi, Y. Horie, M. Bagheri, A. Faraon, Dielectric metasurfaces for complete control of phase and polarization with subwavelength spatial resolution and high transmission. *Nat. Nanotechnol.* **10**, 937–943 (2015).
23. M. Khorasaninejad, W. T. Chen, R. C. Devlin, J. Oh, A. Y. Zhu, F. Capasso, Metalenses at visible wavelengths: Diffraction-limited focusing and subwavelength resolution imaging. *Science* **352**, 1190–1194 (2016).
24. Y. H. Shih, The physics of ghost imaging, https://arxiv.org/abs/0805.1166 (2008).
25. B. I. Erkmen, J. H. Shapiro, Ghost imaging: From quantum to classical to computational. *Adv. Opt. Photonics* **2**, 405–450 (2010).
26. J. H. Shapiro, R. W. Boyd, The physics of ghost imaging. *Quantum Inf. Process.* **11**, 949–993 (2012).
27. T. B. Pittman, Y. H. Shih, D. V. Strekalov, A. V. Sergienko, Optical imaging by means of two-photon quantum entanglement. *Phys. Rev. A* **52**, R3429(R) (1995).
28. R. S. Bennink, S. J. Bentley, R. W. Boyd, "Two-photon" coincidence imaging with a classical source. *Phys. Rev. Lett.* **89**, 113601 (2002).
29. B. Jack, J. Leach, J. Romero, S. Franke-Arnold, M. Ritsch-Marte, S. M. Barnett, M. J. Padgett, Holographic ghost imaging and the violation of a Bell inequality. *Phys. Rev. Lett.* **103**, 083602 (2009).
30. K. Wang, D.-Z. Cao, Subwavelength coincidence interference with classical thermal light. *Phys. Rev. A* **70**, 041801(R) (2004).
31. F. Ferri, D. Magatti, A. Gatti, M. Bache, E. Brambilla, L. A. Lugiato, High-resolution ghost image and ghost diffraction experiments with thermal light. *Phys. Rev. Lett.* **94**, 183602 (2005).
32. A. Valencia, G. Scarcelli, M. D'Angelo, Y. Shih, Two-photon imaging with thermal light. *Phys. Rev. Lett.* **94**, 063601 (2005).
33. Y. Cai, S.-Y. Zhu, Ghost imaging with incoherent and partially coherent light radiation. *Phys. Rev. E* **71**, 056607 (2005).
34. R. Meyers, K. S. Deacon, Y. Shih, Ghost-imaging experiment by measuring reflected photons. *Phys. Rev. A* **77**, 041801(R) (2008).
35. X.-H. Chen, Q. Liu, K.-H. Luo, L.-A. Wu, Lensless ghost imaging with true thermal light. *Opt. Lett.* **34**, 695–697 (2009).
36. J. Cheng, Ghost imaging through turbulent atmosphere. *Opt. Express* **17**, 7916–7921 (2009).
37. P. Clemente, V. Durán, V. Torres-Company, E. Tajahuerce, J. Lancis, Optical encryption based on computational ghost imaging. *Opt. Lett.* **35**, 2391–2393 (2010).
38. C. Zhao, W. Gong, M. Chen, E. Li, H. Wang, W. Xu, S. Han, Ghost imaging lidar via sparsity constraints. *Appl. Phys. Lett.* **101**, 141123 (2012).
39. B. Sun, M. P. Edgar, R. Bowman, L. E. Vittert, S. Welsh, A. Bowman, M. J. Padgett, 3D computational imaging with single-pixel detectors. *Science* **340**, 844–847 (2013).
40. P. Ryczkowski, M. Barbier, A. T. Friberg, J. M. Dudley, G. Genty, Ghost imaging in the time domain. *Nat. Photonics* **10**, 167–170 (2016).
41. N. Tian, Q. Guo, A. Wang, D. Xu, L. Fu, Fluorescence ghost imaging with pseudothermal light. *Opt. Lett.* **36**, 3302–3304 (2011).
42. H. Yu, R. Lu, S. Han, H. Xie, G. Du, T. Xiao, D. Zhu, Fourier-transform ghost imaging with hard X rays. *Phys. Rev. Lett.* **117**, 113901 (2016).
43. D. Pelliccia, A. Rack, M. Scheel, V. Cantelli, D. M. Paganin, Experimental x-ray ghost imaging. *Phys. Rev. Lett.* **117**, 113902 (2016).
44. R. I. Khakimov, B. M. Henson, D. K. Shin, S. S. Hodgman, R. G. Dall, K. G. H. Baldwin, A. G. Truscott, Ghost imaging with atoms. *Nature* **540**, 100–103 (2016).
45. S. Gan, D.-Z. Cao, K. Wang, Dark quantum imaging with fermions. *Phys. Rev. A* **80**, 043809 (2009).

46. H.-C. Liu, High-order correlation of chaotic bosons and fermions. *Phys. Rev. A* **94**, 023827 (2016).
47. D.-Z. Cao, J. Xiong, S.-H. Zhang, L.-F. Lin, L. Gao, K. Wang, Enhancing visibility and resolution in *N*th-order intensity correlation of thermal light. *Appl. Phys. Lett.* **92**, 201102 (2008).
48. K. W. C. Chan, M. N. O'Sullivan, R. W. Boyd, High-order thermal ghost imaging. *Opt. Lett.* **34**, 3343–3345 (2009).
49. Q. Liu, X.-H. Chen, K.-H. Luo, W. Wu, L.-A. Wu, Role of multiphoton bunching in high-order ghost imaging with thermal light sources. *Phys. Rev. A* **79**, 053844 (2009).
50. J. H. Shapiro, Computational ghost imaging. *Phys. Rev. A* **78**, 061802(R) (2008).
51. O. Katz, Y. Bromberg, Y. Silberberg, Compressive ghost imaging. *Appl. Phys. Lett.* **95**, 131110 (2009).
52. F. Ferri, D. Magatti, L. A. Lugiato, A. Gatti, Differential ghost imaging. *Phys. Rev. Lett.* **104**, 253603 (2010).
53. B. Sun, S. S. Welsh, M. P. Edgar, J. H. Shapiro, M. J. Padgett, Normalized ghost imaging. *Opt. Express* **20**, 16892–16901 (2012).
54. E. J. Candes, J. Romberg, T. Tao, Robust uncertainty principles: Exact signal reconstruction from highly incomplete frequency information. *IEEE Trans. Inf. Theory* **52**, 489–509 (2006).
55. D. L. Donoho, Compressed sensing. *IEEE Trans. Inf. Theory* **52**, 1289–1306 (2006).
56. D. Thapa, K. Raahemifar,V. Lakshminarayanan. Less is more: Compressive sensing in optics and image science. *J. Mod. Opt.* **62**, 415–429 (2015).
57. L. Zhang, M. Xing, C.-W. Qiu, J. Li, Z. Bao, Achieving higher resolution ISAR imaging with limited pulses via compressed sampling. *IEEE Geosci. Remote Sens. Lett.* **6**, 567–571 (2009).
58. L. Zhang, M. Xing, C.-W. Qiu, J. Li, J. Sheng, Y. Li, Z. Bao, Resolution enhancement for inversed synthetic aperture radar imaging under low SNR via improved compressive sensing. *IEEE Trans. Geosci. Remote Sens.* **48**, 3824–3838 (2010).
59. W. Ye, F. Zeuner, X. Li, B. Reineke, S. He, C.-W. Qiu, J. Liu, Y. Wang, S. Zhang, T. Zentgraf, Spin and wavelength multiplexed nonlinear metasurface holography. *Nat. Commun.* **7**, 11930 (2016).
60. L. Wang, S. Kruk, H. Tang, T. Li, I. Kravchenko, D. N. Neshev, Y. S. Kivshar, Grayscale transparent metasurface holograms. *Optica* **3**, 1504–1505 (2016).
61. M. Decker, I. Staude, M. Falkner, J. Dominguez, D. N. Neshev, I. Brener, T. Pertsch, Y. S. Kivshar, High-efficiency dielectric Huygens' surfaces. *Adv. Opt. Mater.* **3**, 813–820 (2015).
62. R. W. Gerchberg, W. O. Saxton, A practical algorithm for the determination of phase from image and diffraction plane pictures. *Optik* **35**, 237–246 (1972).
63. Q. Dai, W. Sha, The physics of compressive sensing and the gradient-based recovery algorithms, https://arxiv.org/abs/0906.1487 (2009).

Acknowledgments

Funding: This work was supported by Engineering and Physical Sciences Research Council (EP/J018473/1); European Research Council Consolidator Grant (TOPOLOGICAL); the Royal Society and the Wolfson Foundation; and Horizon 2020 Action, Project Nos. 734578 (D-SPA) and 648783. S.Z. acknowledges support from the Royal Society. B.Y. acknowledges China Scholarship Council (201306110041). Q.G. acknowledges support from the National Natural Science Foundation of China (grant 11604216). J.S. acknowledges support from China Postdoctoral Science Foundation (grant 2016M600668). C.G. acknowledges support from the National Science Foundation of China (grant 61675054). G.Z. acknowledges support from the National Natural Science Foundation of China (grants 11374235 and 11574240) and the Outstanding Youth Funds of Hubei Province (grant 2016CFA034). G.L. acknowledges support from the Natural Science Foundation of Shenzhen Innovation Committee (grant JCYJ20170412153113701). H.M. and T.Z. acknowledge support from the Deutsche Forschungsgemeinschaft (grant ZE953/7-1). **Author contributions:** H.-C.L. conceived the project and designed the experiments with support from S.Z.; G.Z., H.M., G.L., and T.Z. designed and fabricated the metasurface; H.-C.L. performed the optical measurements with contributions from J.S. and C.G.; H.-C.L. carried out the simulations and analyzed the data with contributions from B.Y. and Q.G.; and H.-C.L. and S.Z. wrote the manuscript with contributions from other authors. **Competing interests:** The authors declare that they have no competing interests. **Data and materials availability:** All data needed to evaluate the conclusions in the paper are present in the paper. Additional data related to this paper may be requested from the authors.

Submitted 5 May 2017
Accepted 8 August 2017
Published 8 September 2017
10.1126/sciadv.1701477

Citation: H.-C. Liu, B. Yang, Q. Guo, J. Shi, C. Guan, G. Zheng, H. Mühlenbernd, G. Li, T. Zentgraf, S. Zhang, Single-pixel computational ghost imaging with helicity-dependent metasurface hologram. *Sci. Adv.* **3**, e1701477 (2017).

Science Advances

Single-pixel computational ghost imaging with helicity-dependent metasurface hologram

Hong-Chao Liu, Biao Yang, Qinghua Guo, Jinhui Shi, Chunying Guan, Guoxing Zheng, Holger Mühlenbernd, Guixin Li, Thomas Zentgraf and Shuang Zhang

Sci Adv **3** (9), e1701477.
DOI: 10.1126/sciadv.1701477

Science Advances (ISSN 2375-2548) is published by the American Association for the Advancement of Science, 1200 New York Avenue NW, Washington, DC 20005. The title *Science Advances* is a registered trademark of AAAS.